

## Static and flowing regions in granular collapses down channels: Insights from a sedimenting shallow water model

Emma E. Doyle

*Centre for Environmental and Geophysical Flows, Department of Earth Sciences, University of Bristol, Wills Memorial Building, Queen's Road, Bristol BS8 1RJ, United Kingdom*

Herbert E. Huppert

*Institute of Theoretical Geophysics, Department of Applied Mathematics and Theoretical Physics, Centre of Mathematical Sciences, University of Cambridge, Wilberforce Road, Cambridge CB3 0WA, United Kingdom*

Gert Lube

*Research Division "Dynamics of the Ocean Floor," IFM-GEOMAR, Leibniz Institute for Marine Sciences, Wischofstr. 1-3, D-24148 Kiel, Germany*

Heidy M. Mader and R. Stephen J. Sparks

*Centre for Environmental and Geophysical Flows, Department of Earth Sciences, University of Bristol, Wills Memorial Building, Queen's Road, Bristol BS8 1RJ, United Kingdom*

(Received 20 November 2006; accepted 11 July 2007; published online 2 October 2007)

A two layer model for the collapse and spreading of a granular column is presented. This model builds upon that of Larrieu *et al.* [J. Fluid Mech. **554**, 669 (2006)] where the free fall collapse of the column and subsequent flow of material onto a plane is represented by a "raining" mass source term into a thin flowing layer of constant density. These modified shallow water equations with Coulomb friction capture the free surface of the flows and key scaling laws for initial sand columns of aspect ratios up to  $a < 10$ . However, unrealistically high coefficients of friction of  $\mu = 0.9$  are required to reproduce run-outs observed. Key scaling laws for high aspect ratio columns are also not captured. We thus extend the model of Larrieu (2006) to include an estimation for the interface between the static and flowing regions observed within granular collapses in the laboratory by Lube *et al.* [Phys. Fluids **19**, 043301 (2007)]. An empirical sedimentation term  $L_s$  and the instantaneous removal of a static deposit wedge, seen in the laboratory, are incorporated into the "raining" shallow water model. The growing static deposit surface provides a basal topography for the flowing layer. For a constant empirical sedimentation rate of  $L_s = 0.20$  m/s, a coefficient of friction of  $\mu = 0.4$  simulates comparable run-outs to laboratory observations. The correct run-out dependence of  $a^{2/3}$  for columns of aspect ratio  $a > 3$  is also captured. Simulating this behavior for values of  $a$  above 10 has not been possible with previous continuum models. In addition, this model captures the correct dependence of final run-out time upon  $a^{0.5}$ . The application of this extends beyond observed and simulated collapses, to sedimenting highly concentrated debris flows, useful in the development of large mechanistic numerical models utilized in hazard assessment. © 2007 American Institute of Physics. [DOI: 10.1063/1.2773738]

### I. INTRODUCTION

The understanding of free surface granular avalanches is a fundamental problem in the natural world and in industry. Granular column collapses involve the collapse of a tall column of grains, released from rest in either axisymmetric or two-dimensional geometries. In nature, hazardous granular avalanches occur in the form of snow avalanches, debris flows, pyroclastic flows, landslides, and cliff collapses. The physics of these granular column collapses is much less well understood than their fluid counterparts, involving unsteady behavior with transitions between static and flowing states.

Laboratory investigations into granular column collapses by Lube *et al.*,<sup>1</sup> Lajeunesse *et al.*,<sup>2</sup> and Balmforth and Kerswell,<sup>3</sup> show an initial acceleration stage, followed by a constant velocity phase for high aspect ratio flows and a final deceleration stopping stage.<sup>4</sup> The constant velocity stage is

similar to the slumping phase of a fluid gravity current. Lube *et al.*<sup>1</sup> and Lajeunesse *et al.*<sup>2</sup> independently inferred empirical scaling laws for the run-out, deposit morphology and timescales dependent on the initial aspect ratio of the column,  $a = h_o/x_o$ , height  $h_o$ , and lock-width  $x_o$  (2D planar). Observations by Lube *et al.*<sup>1</sup> indicate that flow kinematics are independent of friction, which only becomes important in the final stages of avalanche emplacement.

Numerical simulations of granular flows range from discrete element simulations<sup>5-7</sup> to continuum models.<sup>8,9</sup> Simplifications come from assuming no vertical variations, resulting in the depth averaged shallow-water equations. These are commonly applied with a Coulomb basal friction law,<sup>10</sup> which is a leading order parameter in the characteristics of the final stopping phase and deposit.<sup>11</sup> These continuum models are important for hazard assessment, as they allow for large scale simulations over natural terrains with existing

computational power. However, they are limited at present by an inability to capture unsteady flow behavior.

Recent numerical models of granular column collapse for both discrete element grain simulations<sup>5-7</sup> and shallow water continuum approximations<sup>12,13</sup> reproduce the key experimental scaling laws. However, in general these models fail to capture some of the main features of the flows. For high values of aspect ratio, the shallow water assumptions are invalid and depth averaging leads to an incorrect representation of the initial column and its effect on the spreading phase.<sup>6,13</sup> To address this problem, Larrieu *et al.*<sup>14</sup> consider first the free fall of the initial column as it collapses. This provides a “raining” mass source into a thin layer within the lock region, described by the shallow water equations. This approach captures the behavior and scaling laws of high aspect ratio columns.

There are limitations with the raining model. First, an unrealistically high value for the coefficient of friction of  $\mu=0.9$  (corresponding to a dynamic friction angle of  $\delta=42^\circ$ ) is required to calibrate the simulations of the total run-out with laboratory observations. However, laboratory measurements<sup>15</sup> give much lower dynamic friction angles,  $\sim 30^\circ$ . Second, run-out scaling laws fail for tall columns where  $a \geq 10$ . Third, this model captures only the evolution of the free surface of the flow and its horizontal motion, with no vertical variations. However, laboratory investigations<sup>1,2</sup> of granular avalanches have identified static and flowing regions in these flows.

Lube *et al.*<sup>16</sup> demonstrated that as granular flows propagate, the interface between static and flowing regions consumes the flowing layer. The flows stop when this interface reaches the free surface. This behavior cannot be captured in the depth-averaged shallow-water models. This sedimentation process is one of the most intriguing properties of granular media and its relationship to run-out is explored further in this numerical study. The physical parameters of natural geophysical flows are often inferred from qualitative interpretations of their deposits and thus understanding this sedimentation is important to assess their hazards.

In this paper we simulate granular column collapses by building upon the model of Larrieu *et al.*<sup>14</sup> In a similar manner to Gray,<sup>17</sup> we model both the static and flowing regions of the collapse by implementing an empirical sedimentation term with topography. This sedimentation represents the rise of the static region surface, and its effect upon the ability of the model to capture key scaling laws with a realistic coefficient of friction is investigated. Observed experimental scaling laws and existing theoretical governing model equations are explained in the next section. Model development then follows in Sec. II with simulations and analysis in Sec. III.

## A. Experimental observations

Analysis of dry granular column collapses and the associated run-out behavior,<sup>1,2</sup> has isolated key empirical scaling laws for the behavior of these collapse flows. Lube *et al.*<sup>1</sup>

found that the run-out distance depends only on the initial aspect ratio of the column and not on the grain size or type, identifying

$$\frac{r_\infty - r_o}{r_o} = 1.24a \quad \text{for } a < 1.7 \quad \text{and} \quad (1)$$

$$\frac{r_\infty - r_o}{r_o} = 1.6a^{1/2} \quad \text{for } a > 1.7,$$

for axisymmetric columns (where the aspect ratio  $a$  equals  $h_o/r_o$ ,  $r_\infty$  representing the final run-out,  $r_o$  the initial radius of the column and  $h_o$  the initial column height) and

$$\frac{x_\infty - x_o}{x_o} = 1.2a \quad \text{for } a < 1.8 \quad \text{and} \quad (2)$$

$$\frac{x_\infty - x_o}{x_o} = 1.9a^{2/3} \quad \text{for } a > 1.8,$$

for 2D channel geometry<sup>4</sup> with  $x_o$  the initial column width and  $x_\infty$  the final run-out. These relationships were found to be independent of material properties<sup>1</sup> for a variety of grain types from sand and cous-cous to rice. Two styles of collapse depend on the initial geometry, with a transition between low ( $<1.8$ ) and high ( $>2.8$ ) aspect ratios. Lajeunesse *et al.*<sup>2</sup> found similar scaling relationships for axisymmetric columns, but with a transitional aspect ratio of 0.74 and prefactor values dependent upon the static angle of repose and thus frictional properties.

Balmforth and Kerswell<sup>3</sup> have confirmed expression (2), with

$$\frac{x_\infty - x_o}{x_o} = \begin{cases} k_x a^{0.9 \pm 0.1} & \text{wide slot} \\ k_x a^{0.65 \pm 0.05} & \text{narrow slot.} \end{cases} \quad (3)$$

They highlight that the constant  $k_x$  depends on the frictional properties of the granular material and the interface with the channel sidewalls. In narrow slot geometry the propagation characteristics are very different to that of a wide slot, due to the greater effect of friction.

Similar scaling laws have also been developed for the final central cone (axisymmetric) or back wall (2D planar) height  $h_\infty$ , found for planar geometry by Balmforth and Kerswell<sup>3</sup> to be

$$h_\infty/h_o \propto a^{0.6} \quad (\text{wide slot}) \quad \text{and} \quad h_\infty/h_o \propto a^{0.5} \quad (\text{narrow slot}), \quad (4)$$

and by Lube *et al.*<sup>4</sup> to be

$$h_\infty/x_o \propto k_h a^{2/5}, \quad (5)$$

$$a > 1.15, \text{ constant } k_h \approx 1 \text{ depending on material,}$$

while for the axisymmetric case

$$\frac{h_\infty}{r_o} = \begin{cases} 0.74 & \text{for } a > 0.74 \text{ (Lajeunesse et al.}^2\text{) and} \\ 0.88a^{1/6} & \text{for } 1.7 \leq a \leq 10 \text{ (Lube et al.}^1\text{),} \end{cases} \quad (6)$$

where for  $a < 0.74$  and  $a < 1.7$  (respectively)  $h_\infty$  is equal to  $h_o$ . For  $a > 10$  a decrease in  $h_\infty$  is observed.<sup>1</sup>

For both axisymmetric and 2D collapses, Lube *et al.*<sup>1</sup> observed that the final run-time scales as  $t_\infty = k_t (h_o/g)^{1/2}$

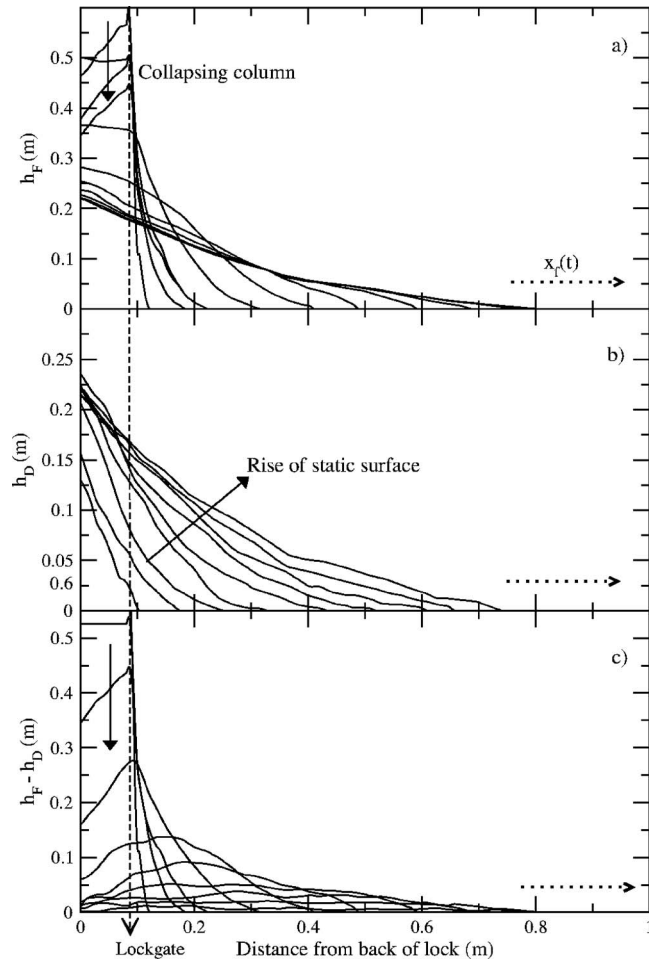


FIG. 1. Laboratory observations of a granular column collapse for aspect ratio  $a=7$  and lock width  $x_o=0.0905$  m, after Lube *et al.* (Ref. 16). (a) The free surface of the collapse flow  $h_F$ , solid arrow indicates column collapse and dotted indicates the front  $x_f$  propagation direction. (b) The interface position between static and flowing regions: the surface of the deposit  $h_D$ . (c) The evolution of the thickness of the flowing layer  $h=h_F-h_D$ . Profiles are shown at time intervals (Ref. 14) of 0.1 s between 0.1 s and the time when the flow front has come to rest and all material is static  $t_{sc}$ , in the future denoted as  $t/t_{sc}=0.1(0.1)1$ .

$=3(r_o/g)^{1/2}a^{1/2}$  with constant  $k_t \approx 3$ , dependent on the initial aspect ratio and material used. These results help identify the key parameters governing these granular collapses in addition to providing a useful tool for validation of numerical models.<sup>3,14</sup>

Figure 1 (after Lube *et al.*<sup>16</sup>) illustrates a typical granular collapse flow, the evolution of the free surface, the growth of the deposit and the thinning of the flowing material layer. An interface between the growing static region and flowing material is approximately parallel to the free surface of the total flow, initiating at the surface of an initial static wedge within the lock region with an angle of  $61^\circ$  (2D case<sup>4</sup>).

The experiments of Lube *et al.*<sup>16</sup> utilize quartz sand of diameter  $1.4 \pm 0.4$  mm. Table I lists angles of repose, basal and internal friction, measured for a variety of materials. Glass beads are considered analogous to smooth quartz,<sup>18</sup> providing the lowest friction values. Thus, the sand of Lube *et al.*<sup>16</sup> is considered as being between the end members of smooth and crushed quartz. The dynamic friction coefficient

is less than the pseudostatic equivalent measured as the angle of repose of a material, which is in turn comparable to values of internal friction.<sup>19,20</sup> Thus we can infer from Table I that the quartz sand has an average basal friction of  $\mu=0.4 \pm 0.2$  with an absolute upper bound of 0.7 as inferred from the angle of repose found by Chik and Vallejo<sup>21</sup> for coarse quartz grains on a glass plate.

## B. Modeling background

Savage and Hutter<sup>8</sup> established the use of depth averaged continuum models in modeling granular flows and debris avalanches. These models assume that the flowing material of constant density  $\rho$  is incompressible. The material is treated as a cohesionless Mohr-Coulomb continuum with an Earth pressure coefficient  $k_a$  and a Coulomb-type basal friction law, arising from the shear stress at the base of the flow. The Earth pressure coefficient relates the stresses normal and parallel to the basal plane, dependent on the internal and basal friction angles. Many models adopt a hydrostatic assumption such that  $k_a \approx 1$ , consistent with experimental results of Pouliquen and Forterre.<sup>10</sup>

The basal friction law is a leading order parameter,<sup>11</sup> controlling the stopping phase and deposit characteristics in numerical simulations. It supplies a dissipation mechanism for dense granular flows<sup>6</sup> and can be viewed as an empirical average of the more complex dissipative processes occurring at small scales within the flow. The Coulomb basal friction law is defined by the ratio of the shear stress  $\tau_{xz}$  to the normal stresses on the basal plane of the flow,

$$\tau_{xz} = -\rho\mu gh = -\text{sgn}(u)\rho gh \tan \delta. \quad (7)$$

The constant friction coefficient,  $\mu = \tan(\delta)$ , defines the critical inclination angle below which uniform steady flow can exist for a smooth plane.<sup>15</sup> An analytical solution for a granular avalanche with a constant friction coefficient has been developed by Mangeney *et al.*,<sup>22</sup> providing a useful tool for model validations.

Pouliquen<sup>15</sup> identified scaling laws for steady uniform granular flows down rough inclines at inclination angles intermediate between static and dynamic friction angles, leading to an alternative empirically determined expression,

$$\mu(u, h) = \tan \theta_1 + (\tan \theta_2 - \tan \theta_1) \exp\left(-\frac{\beta h \sqrt{gh}}{Ld u}\right), \quad (8)$$

where  $d$  is the particle diameter,  $\theta_1$  and  $\theta_2$  represent the range of critical angles over which the flow starts and stops,  $L$  is the characteristic dimensionless thickness over which these angles vary and  $\beta$  is an empirical constant equal to 0.136 independent of bed inclination, roughness and bead size. Here  $\mu$  is not a property of the material but describes instead the interaction between the material and the rough surface. Numerical application of this law has proved successful, but Pouliquen and Forterre<sup>10</sup> state that it is oversimplified for the low velocity regime.

Recently Jop *et al.*<sup>23</sup> have developed a 3D generalization of the friction law, with the use of an internal stress tensor. A yield criterion is found to exist between rigid body and viscoplastic behavior, thus capturing some of the unsteady char-

TABLE I. Values of the dynamic basal friction  $\delta$ , angle of repose  $\theta_r$ , and internal friction angle  $\theta_{\text{int}}$  for various granular media as reported in the literature, where  $d$  represents the average diameter of each grain. Methods of obtaining these values are noted. Note that the corresponding coefficients are defined as  $\mu = \tan \delta$ . The angle of repose used by Carrigy (Ref. 18) can refer either to the angle at which granular media starts to avalanche when rotated in a drum, or the angle of the free surface when avalanching has stopped. We show the latter; the former is a few degrees higher.

$d$ (mm)	Material	$\delta^\circ$	$\theta_r^\circ$	$\theta_{\text{int}}^\circ$	Method
	Glass beads		24		Rotating drum <sup>e</sup>
0.25–0.35			24		Smooth inclined plane <sup>f</sup>
0.5±0.04		24–31			Rough inclined plane <sup>g</sup>
1.26		9–11			Shear gauge, smooth chute flow <sup>h</sup>
3.04		12–15			Shear gauge, smooth chute flow <sup>h</sup>
0.36, 2.94		11–24		18–26	Aluminum flume <sup>i</sup>
	50%/50% mix <sup>a</sup>		29.5		Rotating drum <sup>e</sup>
	Crushed quartz		35		Rotating drum <sup>e</sup>
0.28–0.54	Crushed calcite		36		Smooth inclined plane <sup>f</sup>
2–4	Quartz chips	30		40	Smooth inclined plane <sup>j</sup>
0.10	Quartz sand	20.3	36.71	34.7	Shear test and tilt table. <sup>k</sup> Glass plate
		21.7	37.21	34.7	Very rough porous base
0.10, 1.16	50%/50% mix	15.7	36.75	39.6	Glass plate
		25.4	38.48	39.6	Very rough porous base
1.16	Quartz sand	7.9	33.05	40.7	Glass plate
		29.6	42.17	40.7	Very rough porous base
<0.4	Sand PIP	24.1		27.6	Hubbert-type shear sand box <sup>b,l</sup>
<0.4	Sand SIF	27.4		28.3	Hubbert-type shear sand box <sup>b,l</sup>
0.22–0.4	Sand SHF	25.5		29.2	Hubbert-type shear sand box <sup>b,l</sup>
>0.4	Sand SICI	27.8		27.6	Hubbert-type shear sand box <sup>b,l</sup>
0.38–0.54	Natural sand		35		Smooth inclined plane <sup>f</sup>
0.5–1	Ottawa sand		30.9		Rotating drum <sup>e</sup>
0.5–1	Ottawa sand	25.5±4.5			Rough bed flume <sup>m</sup>
	Dune sand <sup>c</sup>		32.0±0.6		Rotating drum <sup>e</sup>
1.5–2	Sand	29	33		Ring shear test <sup>d,n</sup>
2–3	Sand	30	34		Ring shear test <sup>d,n</sup>
	Polystyrene beads	23.4±2.6			Rough bed flume <sup>m</sup>
	Polystyrene beads	21			Ring shear test <sup>d,n</sup>
1–2	Synthetic zeolite	22.5±1		28±1	Shear box <sup>o</sup>
2–3.5	Plastic beads	27		33	Shear box <sup>o</sup>

<sup>a</sup>Mix of crushed quartz and glass beads.

<sup>b</sup>Stable  $\delta$ . Dynamic value is 4° lower.

<sup>c</sup>Averages across two dunes and USGS flume sand.

<sup>d</sup>Low to medium velocity ring shear test.

<sup>e</sup>Reference 18.

<sup>f</sup>Reference 35.

<sup>g</sup>Reference 10.

<sup>h</sup>Reference 36.

<sup>i</sup>Reference 37.

<sup>j</sup>Reference 38.

<sup>k</sup>Reference 21.

<sup>l</sup>Reference 39.

<sup>m</sup>Reference 19.

<sup>n</sup>Reference 40.

<sup>o</sup>Reference 41.

acteristics of the flow. Because these friction coefficients and appropriate laws are not yet fully understood, most models adopt a constant coefficient Coulomb law (7). Unsteady phenomena in granular flows, such as remobilization, is thus not captured.

Granular column collapses are highly unsteady. Application of depth averaged granular avalanche models has had mixed success. Kerswell<sup>13</sup> and Balmforth and Kerswell<sup>3</sup> found that, while a fixed volume dam break shallow water model captures the frontal shape of laboratory deposits, the majority of the flow remains static because the internal processes are not captured. The full 2D numerical simulations can only capture the scaling laws for low aspect ratio flows.

Differences between the model results and observations, particularly at high aspect ratios, is attributed by Kerswell<sup>13</sup> to incorrect modeling of column collapse, which is observed to collapse undeformed prior to lateral flow.<sup>1,2</sup> These model simulations predict too high a velocity at high aspect ratios,<sup>3,13</sup> which is attributed to both violation of the shallow water assumption and the incorrect theoretical description of the transfer of internal potential energy to kinetic energy required for spreading. Kerswell<sup>13</sup> suggested that the introduction of a more sophisticated velocity-dependent basal drag law may improve the models.

Column collapse can also be modeled by 2D discrete-grain simulations,<sup>6</sup> considering the energy and trajectory of

each individual grain in the column. This has lead Staron and Hinch<sup>6</sup> to reconsider the energy dissipation processes occurring in the collapsing column, utilized by Larrieu *et al.*<sup>14</sup> in their modified depth-averaged model. Additional laboratory observations<sup>1,2</sup> of distinct vertical and horizontal motions of the flow<sup>1,2</sup> led Larrieu *et al.*<sup>14</sup> to consider a two part model, first the vertical free fall collapse of the granular column, and then the resulting horizontal flow.

The flowing layer is described by the shallow water equations with a Coulomb basal friction law. The free fall phase is modelled by the gradual addition of material to the flow within the lock region. This “raining” column is assumed to provide no horizontal momentum. Gradual addition of mass represents a lower input of potential energy due to dissipation<sup>6</sup> than the energy of the initial full column. The following axisymmetric governing equations [for height  $h(r,t)$  and depth averaged velocity  $u(r,t)$ ] describe the incompressible collapse flow of constant density  $\rho$  along distance  $r$ , with time  $t$ :

$$\begin{bmatrix} h \\ hu \end{bmatrix}_r + \frac{1}{r} \begin{bmatrix} ruh \\ rhu^2 \end{bmatrix}_t = \begin{bmatrix} q \\ -\frac{1}{2}k_a g \frac{\partial h^2}{\partial r} - \mu gh \end{bmatrix}. \quad (9)$$

Initial conditions are for a squat thin layer of initial height  $h_i=0.1r_o$  for initial radius  $r_o$ . This initial thickness was chosen by Larrieu *et al.*<sup>14</sup> from the discrete simulations of Staron and Hinch,<sup>6</sup> which indicate that the main part of the column collapses in free fall to a height comparable to the initial radius. If  $h_i \geq 1.5r_o$ , the model fails to capture the correct run-out behavior. Mass supply by raining of the collapsing column is defined as  $q(r,t)=gtH(r_o-r)H(t_r-t)$ ;  $H$  is the standard Heaviside function. Thus, raining only occurs within the initial radius of the column, during the time it takes a grain to fall from the top of the column  $h_o$  to  $h_i$ . The time at which the column is fully collapsed is defined  $t_r = \sqrt{2(h_o-h_i)/g}$ .

There are two key parameters, the Earth pressure coefficient  $k_a$ , which Larrieu *et al.*<sup>14</sup> set to 1 by adopting the hydrostatic assumption and the coefficient of friction  $\mu$ , assumed constant. A value of  $\mu=0.45$  was utilized to compare predicted scaling law exponents with experimental observations. This friction parameter affects the numerical prefactors in these scaling laws. To accurately produce the same scaling law prefactors and thus total run-outs of Lube *et al.*,<sup>1</sup> a very high value of  $\mu=0.9$  is required for the planar models and 0.8 for the axisymmetric case. This limitation is explained by Larrieu *et al.*<sup>14</sup> to arise due to the assumption of depth averaged velocity and the inability of the model to capture vertical velocity variations. These existing models<sup>3,14</sup> can capture the key characteristics of the free surface of these flows and the scaling laws for  $2 \leq a < 10$ . However, they fail to reproduce both the behavior of tall columns and the evolution of the deposit and flowing layers as seen in the laboratory (Fig. 1).

## II. MODEL DEVELOPMENT

Here we expand upon the model of Larrieu *et al.*<sup>14</sup> including the evolution of the static and flowing layers and the interface between them, in the manner of Gray<sup>17</sup> and Douady *et al.*<sup>24</sup> We introduce an empirical sedimentation rate from the flowing layer and address both the issues of high friction and the accurate capturing of key scaling laws for tall columns,  $a \geq 10$ . Our model is composed of a free fall column and a flowing granular layer of constant density  $\rho$ , which thins due to the inclusion of an empirically determined sedimentation rate. The topography at the base of the flowing layer is modified as the deposit grows.

We justify the use of the depth average assumption following Ungarish and Huppert<sup>25</sup> by our assumption that the current has a high constant concentration and bulk density. As stated by Larrieu *et al.*,<sup>14</sup> experiments indicate that the velocity profile varies within the flow. Experiments by Lube *et al.*<sup>16</sup> also show a constant shear at the base of the flow. The shallow-water equations cannot solve for this vertical velocity profile and thus as of Larrieu *et al.*,<sup>14</sup> we utilize a plug flow velocity profile and will show that addition of sedimentation to the governing equations allows for the correct qualitative features of the run-out to be captured.

In the manner of Savage and Hutter,<sup>8</sup> we define the boundary conditions at the base  $b$  and free surface  $f$ :

$$\frac{\partial z}{\partial t} + \frac{u \partial z}{\partial x} - w = q \quad \text{and} \quad \tau_{xz} = 0; \quad z = f(x,t), \quad (10a)$$

$$\frac{\partial z}{\partial t} + \frac{u \partial z}{\partial x} - w = L_s \quad \text{and} \quad (10b)$$

$$\tau_{xz} = -\text{sgn}(\bar{u})\rho gh \cos \theta \tan \delta; \quad z = b(x,t),$$

for distance along slope  $x$  and time  $t$ , where  $z$  is perpendicular to  $x$ . Equation (10a) describes the stress free surface, where  $q$  represents the raining mass source term of the free fall collapsing column, as defined by Larrieu *et al.*<sup>14</sup> in Sec. I A. Equation (10b) describes the empirically observed sedimentation rate  $L_s$  from the base of the flowing layer after Gray.<sup>17</sup> The granular basal shear stress  $\tau_{xz}|_b$  is defined using the Coulomb basal friction law (7) with a constant basal friction angle  $\delta$ .

We depth average the governing conservation of bulk mass for the flowing layer, between the base and free surface, where  $h=f-b$ , by applying the Leibniz integral rule. Defining the vertically averaged velocities as<sup>9,17</sup>

$$(\bar{u}(x,t), \bar{w}(x,t)) = \frac{1}{h} \int_b^f [u(x,z,t), w(x,z,t)] dz \quad (11)$$

and implementing the kinematic boundary conditions (10a) and (10b) leads to the incompressible depth averaged flowing layer mass balance. This is simplified assuming  $\rho$  is constant, resulting in

$$\frac{\partial h}{\partial t} + \frac{\partial \bar{u}h}{\partial x} = q - L_s. \quad (12)$$

Before proceeding with the momentum equation, the depth averaged velocity squared is defined as

$$Sh\bar{u}^2(x,t) = \int_b^f u^2(x,z,t)dz \quad (13)$$

after Hogg and Pritchard.<sup>26</sup> Here  $S$  defines the shape factor, the magnitude of which reflects the shear in the vertical velocity profile of the horizontally flowing layer and is often  $\geq 1$ . Using the standard approach  $S$  is set to unity.

The hydrostatic assumption is adopted by assuming the Earth pressure coefficient  $k_a=1$ , as of Larrieu *et al.*<sup>14</sup> (Sec. I B). This results in a constitutive relation for the hydrostatic pressure  $P$  as a function of  $(x,t)$  (Huppert<sup>27</sup> and Leveque<sup>28</sup>), where

$$\int_b^f Pdz = \frac{\rho gh^2}{2} = \frac{\rho g \cos \theta h^2}{2}. \quad (14)$$

The static growing deposit (arising due to  $L_s$ ) results in a basal topography ( $z_b$ ) and thus the basal pressure boundary conditions for the flowing layer are defined as

$$\frac{\partial z}{\partial x} P = 0 \quad \text{at} \quad z = f(x,t) \quad \text{and} \quad (15)$$

$$\frac{\partial z}{\partial x} P = \frac{\partial z}{\partial x} \rho gh \quad \text{at} \quad z = z_b(x,t),$$

where the granular avalanche of thickness  $h(x,t)$  imposes an overburden pressure at the deposit surface<sup>8</sup>  $z_b$  and the free surface of the flow  $f$  is inferred from  $h+z_b$ .

We integrate the governing conservation of bulk momentum with the property that the stress  $\tau_{xx}=0$  everywhere, due to the bulk Coulomb continuum approximation and include the kinematic (10a) and (10b) and pressure (15) boundary conditions leading to the final depth averaged momentum equation with topography,

$$\begin{aligned} \frac{\partial h\bar{u}}{\partial t} + \frac{\partial(h\bar{u}^2 + 0.5g \cos \theta h^2)}{\partial x} &= gh \sin \theta \\ &- \text{sgn}(\bar{u})gh \cos \theta \tan \delta \\ &- \frac{\partial z_b}{\partial x} g \cos \theta h + \bar{u}(q - L_s). \end{aligned} \quad (16)$$

The inclusion of mass source related terms in the momentum equation is now considered. Larrieu *et al.*<sup>14</sup> assume that the collapse of the column provides only vertical momentum and thereby neglect horizontal momentum. This is based upon observations<sup>1,2,4</sup> that the column experiences an undeformed vertical free fall above a critical height and the discrete grain simulations<sup>6</sup> that show energy dissipation at the base of the collapsing column.

We keep the ‘‘raining’’ horizontal momentum term because the sedimentation induced topography results in the column not falling directly onto a horizontal plane. Deformation of the column below a critical height (found to be  $2.8x_o$  by Lube *et al.*<sup>4</sup>) may also represent horizontal momentum introduced at this stage due to the collapsing of the deformed part of the column. Sedimentation from the flow into the static deposit may not involve purely vertical motion. Analysis of video footage<sup>16</sup> suggests deposit growth involves shearing at the base of the flowing layer. Mass loss, defined by  $L_s$ , may thus remove momentum from the horizontal and the vertical, thus  $\bar{u}L_s$  is retained in Eq. (16). The effect of these momentum flux terms is discussed further at the end of Sec. II and explored in Sec. III D.

*A posteriori* we define an additional mass loss term  $W_s(x)$  describing the initial static wedge seen immediately after lock release.<sup>1-3,16</sup> The model presented here, as of Larrieu *et al.*,<sup>14</sup> starts nonphysically with a prelayer of thickness  $h_i=0.1x_o$  which grows due to raining of the column,  $q$ . When the lock gate is raised at the initiation time  $t_0$ , Lube *et al.*<sup>4</sup> observe a static wedge whose apex exists at  $h/x_o=\tan \theta_w$ , with a wedge front angle  $\theta_w$  of  $61^\circ$ , corresponding to an apex height of 0.16 m for  $x_o=0.09$  m. It is not possible to include this wedge in the layer at  $t_0$  and utilizing a thicker initial layer would violate the shallow water assumption.

We thus model the static wedge as follows. When the flowing layer  $h$  thickens to the observed wedge apex height  $h_c/x_o=\tan \theta_w$ , the wedge area and associated momentum are removed. We assume that sedimentation starts after this. Thus, as of Larrieu *et al.*,<sup>14</sup> we do not capture the deposit and flow profiles during the initial few moments of collapse and focus instead on the subsequent lateral phase of motion, observed by Staron and Hinch<sup>6</sup> to play a dominant role in spreading dynamics.

The final governing equations are defined by (dropping overbars for clarity)

$$\begin{bmatrix} h \\ uh \end{bmatrix}_t + \begin{bmatrix} uh \\ u^2h + 0.5g \cos \theta h^2 \end{bmatrix}_x = \begin{bmatrix} q - k_1L_s - k_2 \frac{W_s(x)}{\Delta t_{rw}} \\ gh \sin \theta - \text{sgn}(u)gh \cos \theta \tan \delta - \frac{\partial z_b}{\partial x} g \cos \theta h + u \left[ q - k_1L_s - k_2 \frac{W_s(x)}{\Delta t_{rw}} \right] \end{bmatrix}, \quad (17)$$

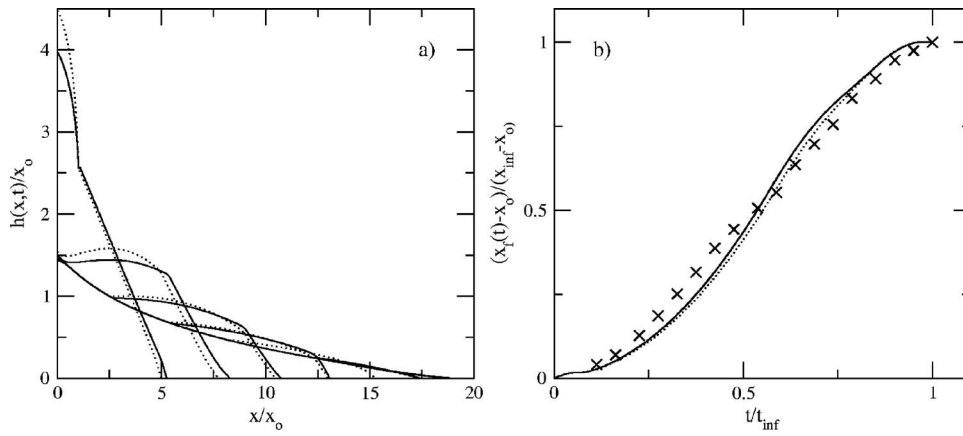


FIG. 2. Validation of our model for no sedimentation,  $L_s=0$  m/s. Inclusion of horizontal momentum corresponding to the collapsing column illustrated in solid lines; simulations without this momentum (dashed lines) directly compare to Larrieu *et al.* (Ref. 14). Initial lock width of  $x_0=0.0905$  m, aspect ratio  $a=7$ , coefficient of friction  $\mu=0.9$ . (a) For the free surface position with time, illustrated at time intervals of  $t/t_{\infty}=0.3(0.1)1$  as of Larrieu *et al.* (Ref. 14). (b) The scaled front position with time, including the observations from experiments (crosses), where  $t_{inf}$  is the time when all material is static with a front position  $x_{inf}$ .

where

$$q = gtH(x_0 - x)H(t_r - t), \quad (18)$$

$$k_1 = H(t - t_w) \quad \text{and} \quad k_2 = \delta'(h - h_c)H(t_w - t), \quad (19)$$

and

$$W_s(x) = (x_0 - x)\tan \theta_w. \quad (20)$$

The time at which the critical height  $h_c$  is reached and the wedge is removed is defined as  $t_w$ . The column collapse is considered complete when  $t=t_r$  is defined in Sec. I B. The value of  $L_s$  and descriptions of the wedge profile are discussed further in Sec. III. The time taken for the wedge to be deposited is defined as  $\Delta t_{rw}$  and set to 1 to represent an instantaneous removal. Note that here  $\delta'(x)$  represents the standard Dirac delta function.

### A. Numerical method

The governing depth averaged Eq. (17) is solved using the finite volume method, an approach commonly adopted for the shallow water equations. We utilize the first order upwind Godunov method.<sup>28</sup> While the wave field of the solution can be further refined by the inclusion of flux limiters leading to higher order resolution methods,<sup>28,29</sup> it is more important to capture the correct solution than refine the wave field [R. P. Denlinger (personal communication, April 26, 2005)]. In addition, as stated by Larrieu *et al.*:<sup>14</sup> “keeping to the first-order scheme enables the model to cope with shock waves generated through the addition of mass with no further numerical refinements.” Full details of this method are found in Leveque.<sup>28</sup>

The first-order Godunov wave-propagation method does not require the entire structure of the Riemann solution and thus we utilize the standard Roe solver<sup>28</sup> after Mangeney *et al.*,<sup>22</sup> Denlinger and Iverson,<sup>29</sup> and Larrieu *et al.*<sup>14</sup> The Roe solver cannot solve a purely dry dam break solution and so, as is standard practice, we apply a stationary negligible prelayer to our model of thickness  $\epsilon=10^{-8}$  m to prevent non-physical solutions when  $h=0$ . The source terms are solved after the main dam break problem, by using a fractional step method. In order to capture the correct wave speed we apply the TRBDF2 method,<sup>28</sup> composed of a 2 step Runge-Kutta and implicit Trapezoid BDF method.<sup>30</sup>

The numerical code, developed in C++, is based upon a series of numerical FORTRAN algorithms developed by Leveque.<sup>28</sup> A standard grid of 2 m has a cell size of  $\Delta x=10^{-3}$  m. An adaptive time step routine based on the Courant, Friedrichs, and Levy condition,<sup>28</sup> is used to decrease simulation runtimes. In this, a maximum time step of  $\Delta t_{\max}=10^{-2}$  s is imposed, but most solutions utilize an average of  $\Delta t=10^{-3}$  s. The flowing layer is controlled by a minimum thickness of  $10^{-4}$  m.

When  $\theta=0$  and the source terms are negligible, the equations are identical to the classic shallow-water dry dam break solution,<sup>28</sup> against which our code has been validated. Including friction in a simulation with a grid resolution of  $\Delta x=0.1$  on a slope of  $\theta=30^\circ$  with  $\delta=10^\circ$ , we recover the analytical results of Mangeney *et al.*<sup>22</sup> to an accuracy of 2.5% for the run-out. As the grid coarsens to 5 m this increases to 5%. Computation times are short so we utilize the finer grid spacing for all our simulations.

Calculation of the sedimentation induced topography term requires special attention. We adopt the flux difference splitting method of Hubbard and Garcia-Navarro<sup>31</sup> to include this spatial source in the finite volume method.<sup>32,33</sup> In this method the spatially varying source terms are decomposed in a manner similar to the main finite volume dam break step, ensuring that the appropriate equilibria of the underlying mathematical model are maintained by the numerical scheme. This has been successfully applied to depth averaged debris avalanches by Denlinger and Iverson.<sup>29</sup> Considering test cases discussed by Leveque,<sup>32</sup> Hubbard and Garcia-Navarro<sup>31</sup> and Caleffi *et al.*<sup>33</sup> we successfully validate the inclusion of the basal topography term into our model equations, but this is not shown here for brevity.

Further validation is conducted against the model of Larrieu *et al.*<sup>14</sup> for a “raining” collapse flow with no sedimentation. Figure 2 illustrates results from our model and the 2D planar version of Eq. (9). Both the height and velocity profiles simulated for  $\mu=0.9$  are validated, the height profile of which [Fig. 2(a)], without momentum relating to the collapsing column  $qu$ , can be compared directly to Fig. 5 of Larrieu *et al.*<sup>14</sup> This raining momentum flux ( $qu$ ) only affects the profiles during the first stages of collapse, with a slightly higher free surface. The total run-out distance is affected by less than 0.5%, well within the error bounds of these simu-

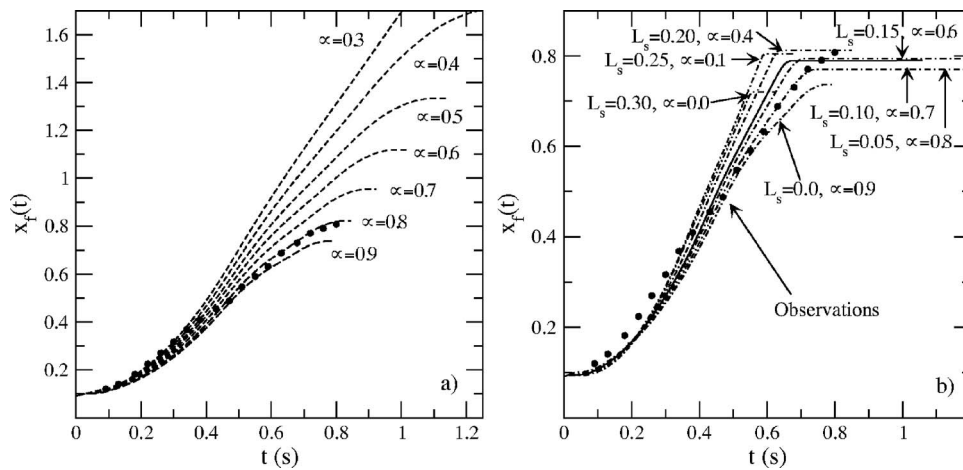


FIG. 3. Observed front position with time for a series of simulations governed by Eq. (17). (a)  $L_s=0$ , varied coefficient of friction,  $\mu$ . Compares to Larrieu *et al.* (Ref. 14). Experimentally observed front positions are shown by black dots (Ref. 16). (b) Varied sedimentation rate  $L_s$  and coefficient of friction,  $\mu$ ; for  $L_s=0(0.05)0.4$  and  $\mu=0(0.1)0.9$ . Simulated run-outs closest to observed experiments are illustrated.

lations. The scaled velocity is only slightly increased in the earlier stages of propagation. The difference between the simulations with and without this momentum flux term are negligible when compared to the overall differences between the simulated and observed run-outs [Fig. 2(b)].

### III. MODEL INVESTIGATIONS

#### A. Constant sedimentation, $L_s$

Lube *et al.*<sup>16</sup> calculated the rate at which the deposit surface rises as  $\partial h_D(x,t)/\partial t$ . Experimental values of this are used as estimates for the sedimentation rate  $L_s$  employed in these simulations. For a representative experiment, with  $a=5$  and  $x_o=0.09$  m, this is found locally<sup>16</sup> to be constant during the free fall phase of the column in the range 0.25–0.33 m/s. When all vertical motion of the column is complete, the flow enters a purely lateral spreading phase, where there is also a constant sedimentation rate of the static layer with time, in the range of 0.12–0.16 m/s for an experiment with  $a=7$ . These local rates are observed to be independent of local flow depth and velocity.

To simulate these quartz sand experiments we initially assume no static wedge and utilize a constant  $L_s$  in Eq. (17), for lock width  $x_o=0.09$  m and  $a=7$ . In some circumstances, such as flow on an inclined plane, erosional regimes may exist where deposited material becomes remobilized. This would not be described by a constant sedimentation rate. However, the model presented here focuses on the run-out and deceleration of the flows in the horizontal, for which detailed experimentation exists and constant sedimentation is observed.<sup>16</sup>

We consider first the case of no sedimentation  $L_s=0$  as of Larrieu *et al.*,<sup>14</sup> illustrated in Fig. 3(a) for  $\mu=0-0.9$ . Decreasing  $\mu$  increases both the velocity of the flow and its final front position. As in Larrieu *et al.*,<sup>14</sup> a simulated run-out of 0.82 m is closest to observations of 0.81 m obtained with a high value of friction ( $\mu=0.8$ ). Larrieu *et al.*<sup>14</sup> however assumed a value of  $\mu=0.9$ , corresponding to a dynamic friction angle of  $42^\circ$ , to reproduce the scaling laws discussed in Sec. I A. For a value of  $\mu \approx 0.4$  ( $\delta=22^\circ$ ), representative of values measured independently in laboratory experiments (Table I, Sec. I A), the calculated run-out of 1.71 m is twice that observed. The decrease from  $\mu=0.9$  to the representative

$\mu=0.4$  results in a factor 2.3 increase in run-out distance and 1.7 in propagation time compared to observations.

The observed run-out is approximately reproduced by a variety of values of  $\mu$  and  $L_s$  [Fig. 3(b)], which appear to have an inverse correlation. While these parameters are intrinsically related, the choice of their values is still crucial. If  $\mu$  is too high with a low  $L_s$  a final en masse freezing is simulated, which is not what is observed. Conversely, if  $L_s$  is too high the final deposit is formed by a rapid accretion of material from the flowing layer resulting in a foreshortened run-out in both time and length.

Taking  $\mu=0.4$ , the experimental observations are most closely matched for  $L_s=0.20$  m/s, a value consistent with the measurements of  $L_s$  in Lube *et al.*<sup>16</sup> Although encouraging, a problem emerges when comparing the model results and observations in terms of the stopping time and the mechanism of stopping. In the model of Larrieu *et al.*<sup>14</sup> the flow stops when all the material comes to rest, a consequence of the friction being the only dissipative term. Here friction and sedimentation are taken as independent parameters and a time-scale discrepancy emerges in the model runs. For example, for  $L_s=0.20$  m/s and  $\mu=0.4$  (our best match to the experiments) the flow front stops at a time of 0.64 s, but at this time the flowing layer still exists and sedimentation finishes at 0.85 s. The problem is further illustrated in Fig. 4 for the extreme case  $L_s=0.05$  m/s and  $\mu=0.8$ . When the flow front stops, at a time herein defined as  $t_{xf}$ , there remains a large amount of unsedimented material [shaded region in Fig. 4(e)].

We investigated reducing the time difference between the flow front stopping ( $t_{xf}$ ) and sedimentation ceasing at  $t_\infty$ . The final sedimentation time is always greater than the flow stopping time. The presence of  $\mu$  and the momentum loss term  $uL_s$  [Eq. (17)], reduces the momentum of the flow in a shorter time than that needed for the sedimentary material into the static region. If  $\mu$  is negligible and the sedimentation rate is increased to  $L_s=0.40$  m/s, the time difference is reduced to 0.06 s. However, the run-out distance is shortened considerably to 0.59 m compared to the observation of 0.81 m. In addition, the values of  $\mu$  and  $L_s$  used to obtain this result are not comparable to observations. These results are thus inconsistent with the experimental observations,

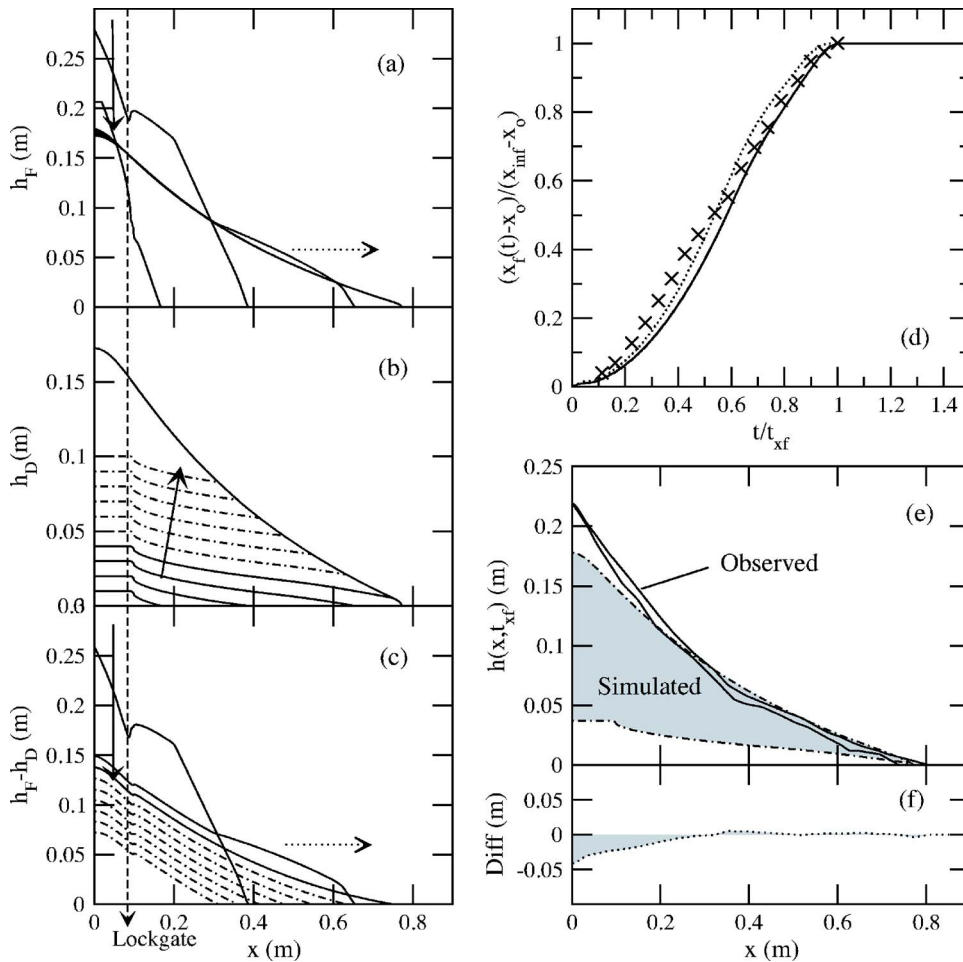


FIG. 4. (Color online) Numerical simulations for  $a=7$ ,  $\mu=0.8$ , and constant  $L_s=0.05$  m/s. (a) The free surface  $h_F$ ; (b) the deposit (or internal) surface  $h_D$ ; and (c) the thickness of the flowing layer  $h_F-h_D$ . Profiles at  $t/t_\infty = 0.3(0.1)1.0$ . (d) The scaled front position (solid) with respect to the time, where  $x_{inf}$  is the final front position and  $t_{xf}$  the front stoppage time. This is compared to a simulation of  $\mu=0.9$ ;  $L_s=0$  m/s (dashed) and experiments (crosses). (e) Comparison of the observed and simulated final deposits. Solid lines illustrate the free surface (top line) and deposit (lower line) at the point at which the flow front becomes stationary  $t_{xf}$ . Almost immediately after, both profiles are equal at  $t_\infty$ . Dashed lines illustrate the simulated profiles at  $t_{xf}$ . The shaded region represents undeposited material at  $t_{xf}$ , due to a high  $\mu$  stopping the flow before it is fully deposited (due to low  $L_s$ ). (f) The difference between the free surfaces for the observed and simulated collapse. Note that the dashed lines in (b) represent the sedimentation  $L_s$  occurring after  $t_{xf}$ . run-out distance:  $x_\infty=0.771$  m and times:  $t_{xf}=0.737$  s and  $t_\infty=2$  s.

which show that the flow stops when the sedimentation interface reaches the free surface. Thus, while the model reproduces the observed run-outs at values of  $\mu$  consistent with experimental measurements it retains unphysical features.

Our best match ( $L_s=0.20$  m/s and  $\mu=0.4$ ) to experimental observations is a balance between the closest propagation distance  $x_\infty$  and the front stopping time  $t_{xf}$  which has the shortest time discrepancy to  $t_\infty$ . Thus, while the upper bound on representative friction values of  $\mu=0.6$  produces the closest velocity to observations when a value of  $L_s=0.15$  m/s is imposed [Fig. 3(b)], it is not chosen as it does not best satisfy these criteria.

These initial simulations demonstrate that including an empirical sedimentation term allows a more realistic coefficient of friction to replicate the run-out observed in the laboratory. This addresses the limiting requirement of a high coefficient of friction ( $\mu=0.9$ ) required in the model of Larrieu *et al.*<sup>14</sup> while also reducing the sensitivity of the simulated model run-out to the  $\mu$  value used.

## B. The static wedge, $W_s$

We now investigate the role of the static wedge, observed in experiments<sup>16</sup> (Fig. 1) but neglected in the first model. Simulations for an aspect ratio of  $a=7$  were conducted utilizing Eqs. (17) and accepting that the static and flowing region profiles during the initial few moments of

column collapse will not be captured. Results for a static wedge angle of  $\theta_w=61^\circ$ , sedimentation rate of  $L_s=0.25$  m/s, and imposed friction  $\mu=0.45$  are illustrated in Figs. 5(a)–5(f). The time discrepancy between the time the flow front stops  $t_{xf}$  and the sedimentation cessation time  $t_\infty$  is improved relative to simulations without a wedge, being reduced to 0.10 s.

The presence of the static wedge has also somewhat improved the flowing layer and deposit profiles of the collapse flow [Figs. 5(a)–5(c)]. The slope of the introduced wedge and the presence of the topography term  $(\partial z_b / \partial x)g \cos \theta h$  in Eq. (17) has resulted in a thinning of this layer at the back of the lock, as observed [Fig. 1(c)]. However, the final back wall deposit height is a little larger than observations [Fig. 5(b),  $h_\infty=0.24$  m versus Fig. 1(b), 0.22 m], most likely due to an oversteep wedge. There is also an unphysical break in slope in the deposit and free surface profiles, corresponding to the sharp topography change at the front of the introduced wedge and the initiation of sedimentation at a precise time.

Observations and simulations of the free surface, flowing layer and deposit profiles at distinct times are illustrated in Fig. 6. For a lock-width of  $x_0=0.09$  m, the critical height  $h_c$  is reached at 0.18 s, denoted by the time  $t_w$ . At this time, the wedge removed in the model [Fig. 6(e)] is narrower, extending to only 0.09 m, than the observed static deposit [Fig. 6(b)] which extends to 0.15 m. In addition the observed de-

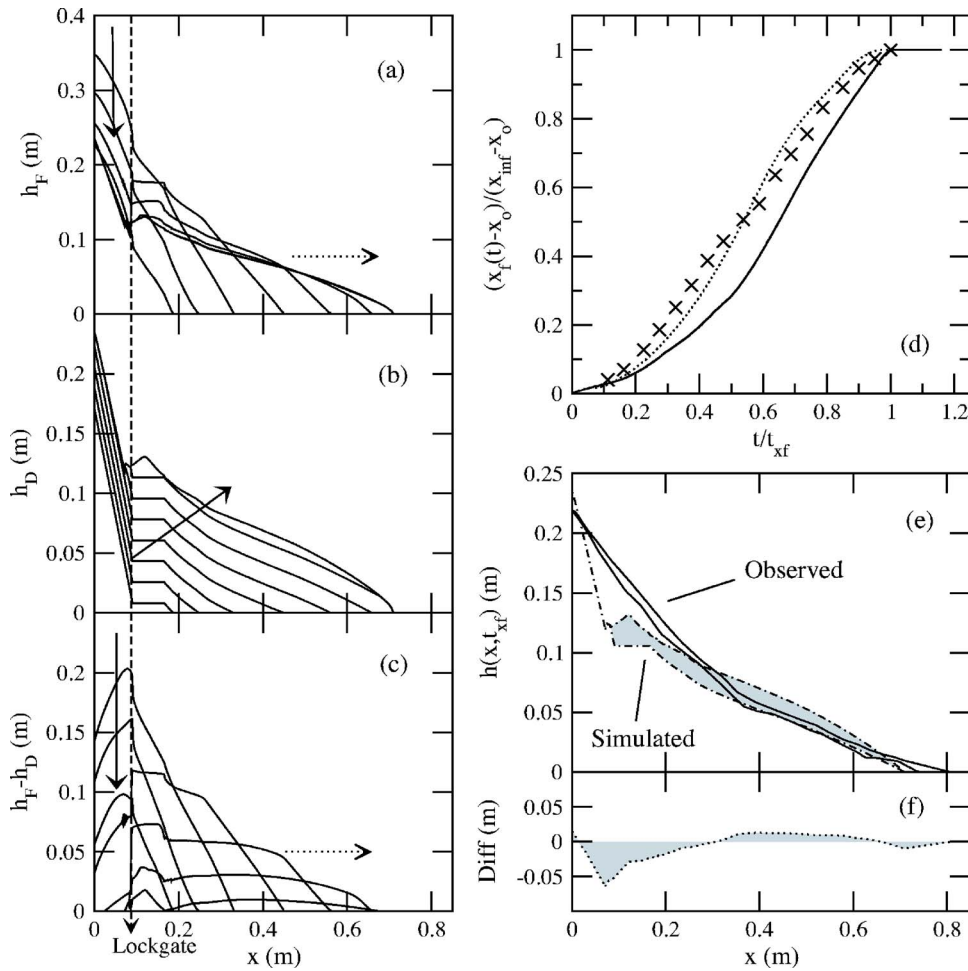


FIG. 5. (Color online) Numerical simulations including an initial straight static wedge in the lock.  $L_s = 0.25$  m/s,  $\mu = 0.45$ , and  $a = 7$ . The wedge of angle  $\theta_w = 61^\circ$  is removed when flow thickness reaches the apex height, the time of which is denoted by  $t_w$ . Key as in Fig. 4. run-out distance:  $x_\infty = 0.709$  m and times:  $t_{xf} = 0.604$  s and  $t_\infty = 0.700$  s.

posit has a curved surface compared to the modelled wedge, resulting in the increased discrepancies between simulations [Fig. 6(f)] and observations [Fig. 6(c)] at later times. Alternative trial simulations, including investigations of a damping function on the sedimentation and a smaller wedge of lower angle, have not removed these differences. We thus reconsider our wedge removal function (20) introducing a curved wedge surface more representative of the deposit observed at the time of removal.

### C. Utilizing the curved static wedge model

We introduce a curved wedge whose apex exists at  $h_c$  and front at  $x_{wf}$ , which coincides with the flow front  $x_f(t_w)$  at the time of removal. The angle of the wedge is not set *a priori* and varies with  $x$ . The wedge is steepest at the back of the lock and shallowest at the wedge front. The height of the curved wedge  $W_s$  with distance from the back of the lock  $x$ , is defined by a triangle existing between  $x$  and  $x_{wf}$ , the front angle of which is defined as  $\theta_w^{xf}(x)$ . The removed wedge profile is thus defined by

$$W_s(x) = (x_{wf} - x) \tan \theta_w^{xf}(x). \quad (21)$$

The angle  $\theta_w^{xf}(x)$  thus represents the angle of the curved wedge tangent at that point, defined by

$$\theta_w^{xf}(x) = \theta_w^{xf}(0) - x \left( \frac{\partial \theta_w^{xf}}{\partial x} \right), \quad (22)$$

where  $\partial \theta_w^{xf} / \partial x$  represents the change of the corresponding front angle with  $x$ , from the largest triangle at  $\theta_w^{xf}(0)$  to the smallest at  $\theta_w^{xf}(x_{wf})$ .  $\theta_w^{xf}(0)$  thus corresponds to the steepest part of the curved wedge at the back of the lock and is defined by  $\theta_w^{xf}(0) = \tan^{-1}(h_c / x_{wf})$ . An assumed wedge curvature is represented by  $k_w$ , where the smallest angle at the very front of the curved wedge is defined by  $\theta_w^{xf}(x_{wf}) = k_w \theta_w^{xf}(0)$ . This leads to a full definition of

$$\theta_w^{xf}(x) = \theta_w^{xf}(0) - \left[ \frac{\theta_w^{xf}(0) - k_w \theta_w^{xf}(0)}{x_{wf}} \right] x. \quad (23)$$

Utilizing  $k_w = 1$  in expression (23) thus represents a straight wedge to be removed. Meanwhile for  $k_w = 0$ , the wedge is highly curved with a front whose surface angle equals the plain in front of it.

Figure 7 illustrates curved wedge profiles when  $h_c = x_o \tan 61^\circ$  for  $x_o = 0.09$  m for values of curvature from  $k_w = 0$  to 1. A value of  $k_w = 0.25$  produces a wedge profile most similar to the static region observed at  $t_w$  in experimental observations. Test simulations illustrate that the final run-out and propagation time are only slightly affected by this curvature. The discrepancy between  $t_{xf}$  and  $t_\infty$  is marginally

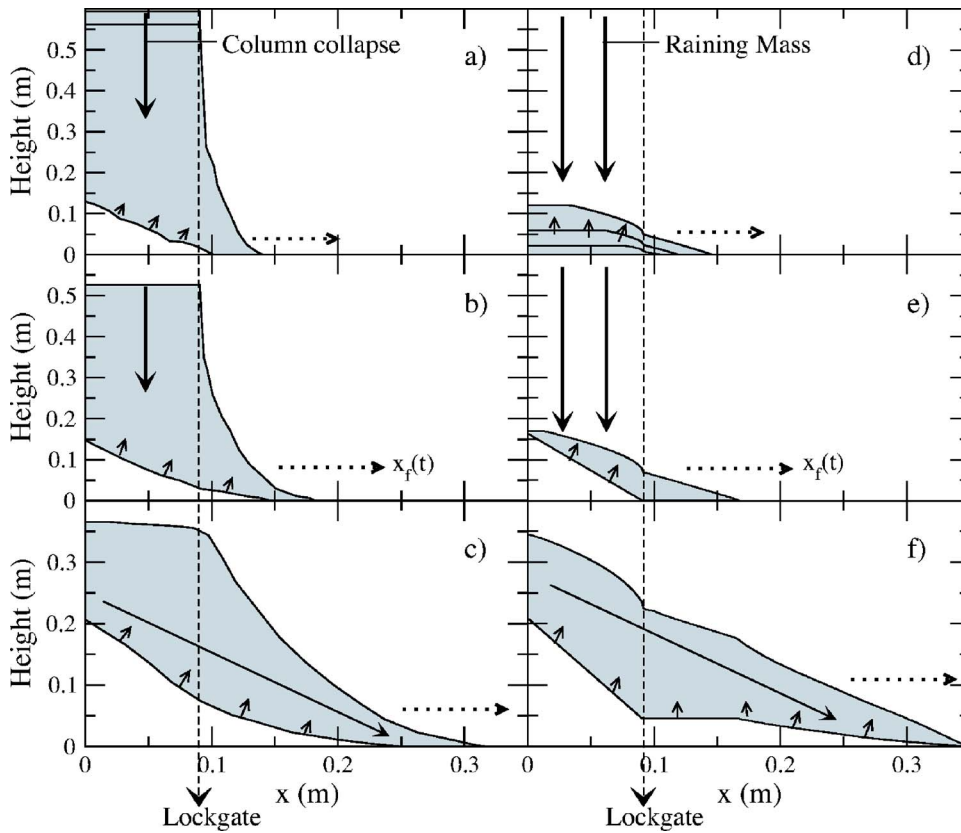


FIG. 6. (Color online) The free surface profiles for laboratory observations (a)–(c) and numerical simulations (d)–(f) of an  $a=7$  column collapse. Shading represents nonstatic material. Laboratory observations: (a) at time  $t=0.05$  s, (b) at time  $t=0.18$  s, and (c) at time  $t=0.36$  s. Corresponding numerical simulations: (d) at  $t=0.05, 0.1, \text{ and } 0.15$  s; (e) at the time of wedge removal  $t_w=0.18$  s, and (f) at the time at which the column has fully collapsed and all motion is lateral,  $t_s=0.36$  s. The initial profiles of the collapse and flow are not captured in our model. These correspond to the time it takes the initial height within the modelled lock,  $h_i$  to reach the critical wedge removal height,  $h_c$ .

changed compared to straight wedge simulations. For  $L_s = 0.20$  m/s and  $\mu=0.4$  it is reduced to 0.08 s. The included curvature term, while not significantly improving run-out position and time relative to the straight wedge, greatly improves the smoothness of the layer profiles. Nonphysical so-

lutions are removed. Simulations discussed herein thus utilize  $k_w=0.25$ , chosen for smoothest results.

Adopting the same approach as for the nonwedge model, a series of simulations were run for  $\mu=0-0.9$  and  $L_s = 0.05-0.40$  m/s using the curved wedge profile expressions (21) and (23). Again, as in Sec. III A, when a coefficient of friction representative of quartz sand ( $\mu=0.4$ ) is imposed, a simulated result closest to that observed<sup>16</sup> is found for  $L_s = 0.20$ , illustrated in Fig. 8. The final simulated run-out of  $x_\infty=0.81$  m is exactly that seen in experiments, while the flow front stopping time is still a little low at  $t_{xf}=0.64$  s compared to the 0.80 s observed. Simulations utilizing a value of  $\mu$  at the upper limit of those representative for quartz sand (Table I) of 0.6, are most comparable to observations when  $L_s=0.15$  m/s. However,  $[t_\infty - t_{xf}]$  is increased to 0.27 s compared to 0.08 s.

Considering these values of  $x_\infty$ ,  $t_{xf}$ , and  $[t_\infty - t_{xf}]$  and the smoother deposit and final profiles [Figs. 8(b), 8(e), and 8(f)], the values of  $L_s=0.20$  m/s when  $\mu=0.4$  are chosen for scaling analysis, discussed in Sec. III E. This best match to observations has also been verified with experimental data for a column of aspect ratio  $a=5$ . These values of  $L_s$  and  $\mu$  are representative of values for the quartz sand used by Lube *et al.*<sup>16</sup> in their experiments, as illustrated in Table I and discussed in Sec. I A. This ability to simulate both the run-out of granular column collapses using friction values representative of natural media and to capture the internal characteristics of the flow, has not been possible with previous depth averaged models.

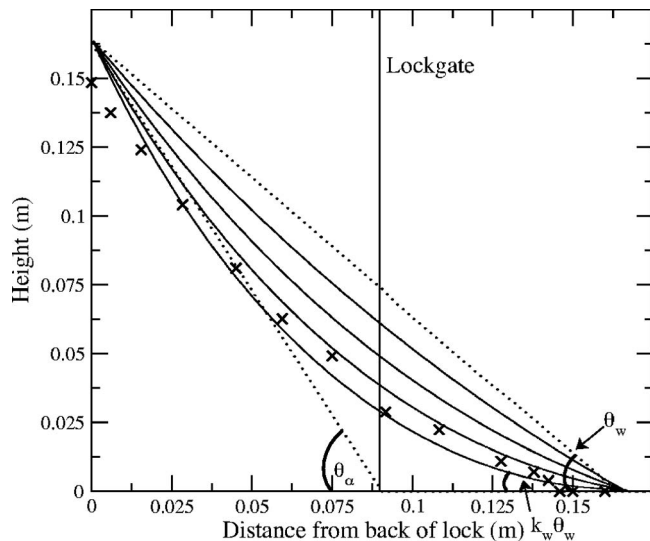


FIG. 7. Different theoretical static wedge profiles. Dashed lines represent a straight wedge ( $\theta_\alpha=61^\circ$ ) within the lock. Solid lines illustrate curved wedges defined by Eqs. (21) and (23), with values of curvature  $k_w=0, 0.25, 0.5, \text{ and } 0.75$  where  $k_w=0$  is the most curved. According to Eq. (23) the wedge is removed when the flow thickness reaches the critical apex height, denoted by the time  $t_w$ . Experimental observations of the static deposit at this time are indicated by crosses, from Lube *et al.* (Ref. 16). Aspect ratio  $a=7$  and lock  $x_p=0.0905$  m.

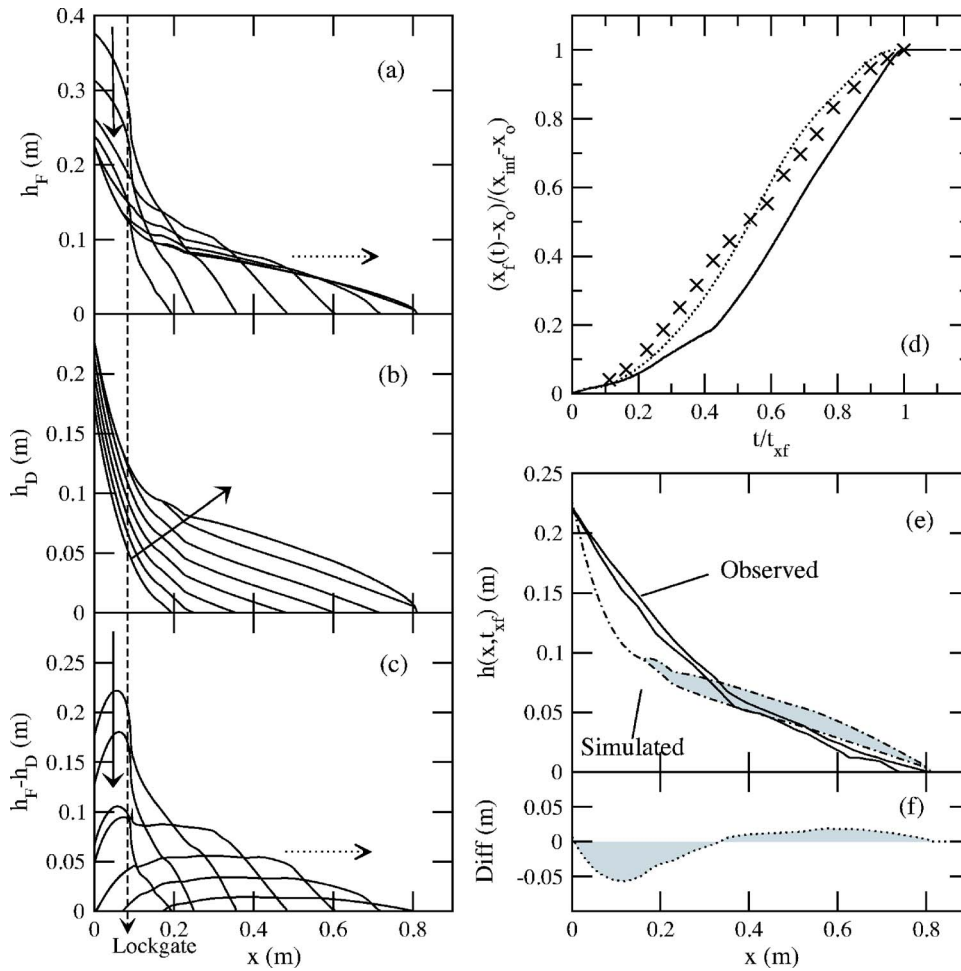


FIG. 8. (Color online) Numerical simulations for a curved wedge.  $L_s = 0.20$  m/s,  $\mu = 0.4$ ,  $a = 7$  and wedge curvature of  $k_w = 0.25$  [Eqs. (21) and (23)]. Wedge apex and critical removal height defined by  $h_c = x_0 \tan 61^\circ$ . Key as in Fig. 4. run-out distance:  $x_\infty = 0.810$  m and times:  $t_{xf} = 0.638$  s and  $t_\infty = 0.719$  s.

**D. Investigating the momentum flux terms**

The effect of the momentum flux terms is now investigated. As discussed in Sec. II, the inclusion of the raining column momentum flux makes less than 0.5% difference to the simulated run-out (Fig. 2). The inclusion of the momentum fluxes associated with sedimentation and wedge removal ( $L_s u$  and  $W_s u$ ) is justified by the experimental observation of a shearing at the base of the flowing layer, below which the static deposit forms<sup>16</sup> (Sec. II), indicating that the sedimentation process may involve horizontal dissipation.

If the “best-fit” result ( $L_s = 0.20$  m/s and  $\mu = 0.4$ ,  $a = 7$ ) is resimulated without these momentum terms, the flow velocity increases. The final run-out position is increased by 7.5%, associated with a decrease of 7% in time. However, the observed flow run-out is captured by increasing  $\mu$  from 0.4 to 0.6 ( $\delta = 21^\circ$  to  $32^\circ$ ) resulting in a 2% difference in final position to the original simulation. This increased friction coefficient is still within the values expected for this granular media (Table I, Sec. I A).

Figure 9 illustrates the unscaled run-out and final deposit

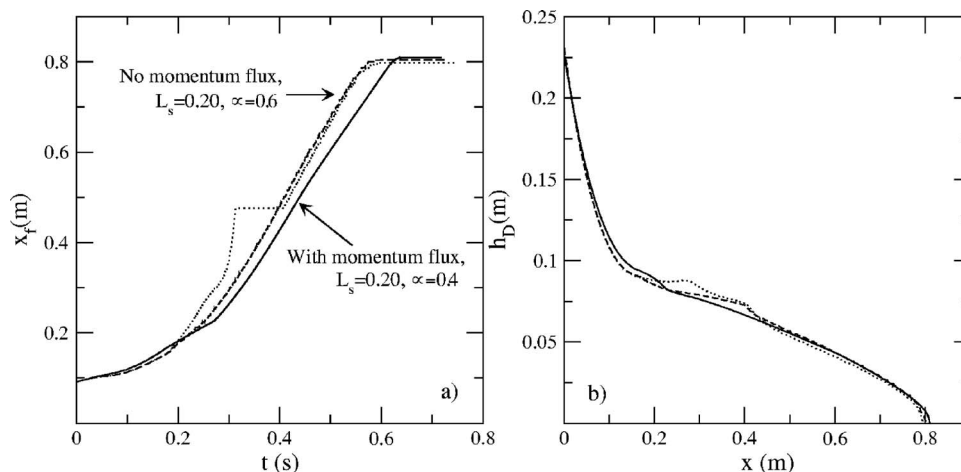


FIG. 9. (a) Unscaled run-out and (b) final deposit profile for the model simulation closest to experimental observations. Results are shown for the model which incorporates all momentum flux terms  $qu$ ,  $L_s u$ , and  $W_s u$  (solid lines), which neglects all these terms (dotted lines) and the model which neglects momentum associated with rain  $qu$  and sedimentation  $L_s u$ , but retains that associated with the static wedge removal  $W_s u$  (dashed lines). Note the exaggeration of the vertical scale in (b).

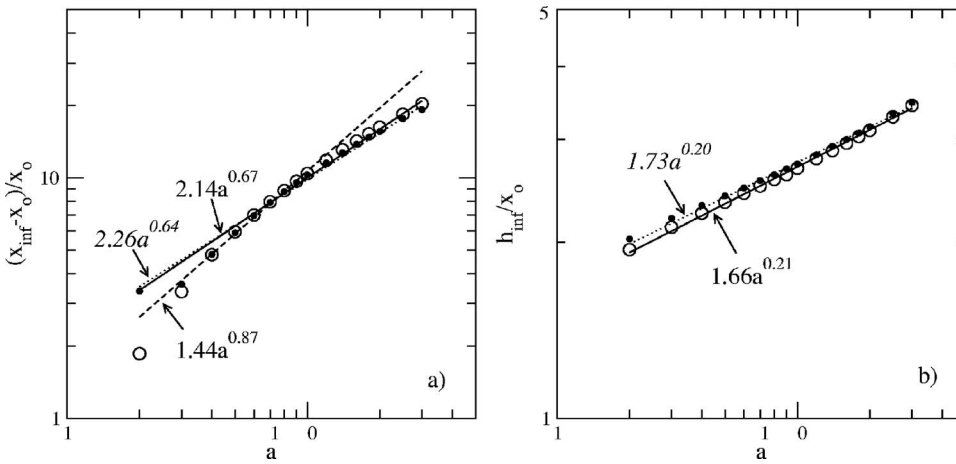


FIG. 10. Key distance and height scaling laws with respect to the aspect ratio  $a$ . Based on simulations with  $L_s = 0.20$  m/s and  $\mu = 0.4$  ( $\delta = 22^\circ$ ). (a) The run-out distance  $x_{inf}$ , normalized by the initial lock width. (b) The final maximum height at the back of the lock  $h_{inf}$ , normalized by the lock width. Power laws are also shown. Results for the model which neglects momentum associated with rain  $qu$  and sedimentation  $L_s u$ , but retains that associated with the static wedge removal  $W_s u$  are also shown (filled circles), with corresponding power laws (dotted lines) indicated in italics.

profile for these simulations with and without these momentum fluxes. Neglecting  $W_s u$ ,  $qu$ , and  $L_s u$  results in unrealistic solutions for 0.2 s after wedge removal [Fig. 9(a)]. This corresponds to a very thin layer (<3 grains) flowing out in front of the bulk of the flow, due to the high momentum of the flow on the wedge topography, before rapidly coming to rest. However a realistic final profile is retained with less than a 1% difference in final run-out time and distance when compared to a model that only neglects  $qu$  and  $L_s u$ .

As the presented model starts with a nonphysical prelayer during the early stages of collapse (Sec. II, Larrieu *et al.*<sup>14</sup>), we retain the wedge removal momentum flux  $W_s u$  for the smoothest flow profiles and focus on the subsequent lateral flow behavior, after wedge removal. These results illustrate that the momentum associated with sedimentation  $L_s u$  has the greatest affect on simulated flow behavior. However, the inclusion of the associated mass flux  $L_s$  still allows for observed flow behavior to be captured with a model that utilizes realistic friction coefficients, with or without this corresponding momentum flux.

**E. Investigating the key scaling laws**

Simple shallow water models for granular column collapses commonly fail to accurately predict the scaling of the run-out and final height, with the classic approach predicting a linear dependence of  $x_\infty$  upon  $a$  due to the friction law imposed.<sup>3</sup> Figure 10(a) illustrates the dependence of simulated run-out upon aspect ratio. For our model we find that above  $a=3$  the scaling law is defined by

$$\frac{x_\infty - x_o}{x_o} = 2.14(\pm 0.13)a^{0.67(\pm 0.02)} \quad \text{and} \tag{24}$$

$$\frac{x_\infty - x_o}{x_o} = 2.26(\pm 0.13)a^{0.64(\pm 0.02)}$$

when momentum flux terms are included or neglected in the model, respectively. This compares to observations by Lube *et al.*<sup>4</sup> of  $1.9a^{0.67}$  for  $a > 1.8$  and by Balmforth and Kerswell<sup>3</sup> of  $k_x a^{0.65(\pm 0.05)}$  for a narrow slot experiment. If  $\mu = 0.45$ , Larrieu *et al.*<sup>14</sup> found a prefactor of 4.4 from their simulated results and thus they required  $\mu = 0.9$ . However, we are able to capture this scaling law and a comparable prefactor to

observations, with simulations that use a value of  $\mu = 0.4$ , or  $\mu = 0.6$  when momentum flux terms are neglected, both of which are representative of quartz sand.

A weaker fit is observed in the simulations below  $a=4$  where  $1.44(\pm 0.09)a^{0.87(\pm 0.03)}$ . At these lower aspect ratios, the static wedge removed from the flowing layer has a greater affect on the subsequent run-out and profiles of the flow. When  $h_c = x_o \tan 61^\circ$ , the apex of the wedge corresponds to an aspect ratio of 1.8. Thus, for  $a=3$  this wedge comprises a greater percentage of the final deposit than for high  $a$  and any misrepresentation of this wedge will be more apparent in the final deposit position. Not incorporating a dependence of  $L_s$  upon  $a$ , suggested a decrease with decreasing  $a$  by Lube *et al.*,<sup>16</sup> may also explain this fit decrease.

The model of Balmforth and Kerswell<sup>3</sup> cannot capture the run-out distance scaling law for tall columns, due to the collapsing column violating the shallow water assumption. The modified two part model of Larrieu *et al.*,<sup>14</sup> on which this model is based, while not violating these assumptions, also fails for  $a > 10$ . Our model captures the empirical laws<sup>4</sup> and corresponding prefactors detailed in Eq. (2) for these tall columns.

Considering the final maximum height found at the back wall of the lock [Fig. 10(b)], we find a dependence of

$$\frac{h_\infty}{x_o} = 1.66(\pm 0.01)a^{0.21(\pm 0.01)} \quad \text{and} \tag{25}$$

$$\frac{h_\infty}{x_o} = 1.73(\pm 0.02)a^{0.20(\pm 0.01)}$$

for  $a \geq 3$ , when momentum flux terms are included or neglected in the model, respectively. These compare to a value of  $k_h a^{0.4}$  for  $a > 1.15$  found by Lube *et al.*<sup>4</sup> and the similar scaling of  $h_\infty/h_o = k_h a^{0.5}$  by Balmforth and Kerswell.<sup>3</sup> The lower power law dependence we observe arises from the higher deposit heights at low  $a$ . A more concave deposit is formed at low  $a$ , the shape of which in the lock region is similar to the static wedge removed. For higher aspect ratios, an oversteep deposit region within the lock still exists, due to the wedge, however its affect is less when considered against the length of the entire deposit. Thus, the misfit of expression

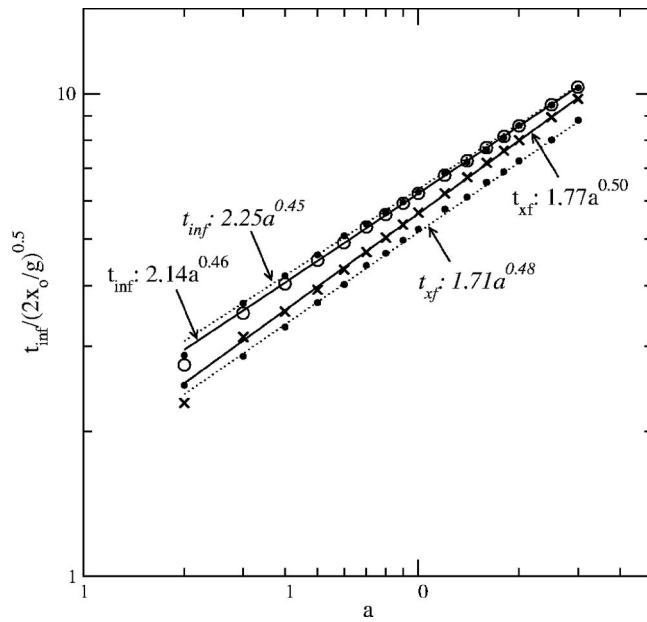


FIG. 11. Key time scaling laws, as a function of  $a$ , for when the flow front comes to rest  $t_{xf}$  and all material has deposited  $t_{inf}$ . Normalized by  $\sqrt{2x_o/g}$  to represent the input of the free fall of the column as of Larrieu *et al.* (Ref. 14). Power laws are shown. Corresponding results for the model which neglects momentum associated with rain  $qu$  and sedimentation  $L_s u$ , but retains that associated with the static wedge removal  $W_s u$  are also shown (filled circles), with power laws (dotted lines) indicated in italics.

(25) may arise due to the form of the static wedge used, particularly for short columns.

The third scaling law of interest is the total run-out time. In their experiments, Lube *et al.*<sup>1</sup> observe  $t_{\infty}/\sqrt{2x_o/g} = 2.12a^{0.5}$  while in simulations Larrieu *et al.*<sup>14</sup> observe  $t_{\infty}/\sqrt{2x_o/g} = 4.35a^{0.36}$ . Figure 11 illustrates the scaling law observed by our simulations for  $t_{xf}$ , the time at which the flow front comes to rest and  $t_{\infty}$  the time at which all material is deposited. When all momentum flux terms are included in the model, the difference between these times decreases with increasing aspect ratio. The sedimentation rate  $L_s$  thus has a greater affect upon flow run-out at lower aspect ratio flows. The scaling laws are

$$\begin{aligned} \frac{t_{\infty}}{\sqrt{2x_o/g}} &= 2.14(\pm 0.01)a^{0.46(\pm 0.01)} \quad \text{and} \\ \frac{t_{\infty}}{\sqrt{2x_o/g}} &= 2.25(\pm 0.02)a^{0.45(\pm 0.01)}, \\ \frac{t_{xf}}{\sqrt{2x_o/g}} &= 1.77(\pm 0.01)a^{0.50(\pm 0.01)} \quad \text{and} \\ \frac{t_{xf}}{\sqrt{2x_o/g}} &= 1.71(\pm 0.02)a^{0.48(\pm 0.01)}, \end{aligned} \quad (26)$$

when momentum flux terms are included or neglected in the model, respectively. These are comparable to the empirical law of Lube *et al.*<sup>1</sup> The slightly low prefactor found for  $t_{xf}$  may arise from the flows propagating too fast in our simulations. However, this model is able to capture the observed law and behavior for tall columns ( $a > 10$ ). The model presented here captures the observed scaling laws with and

without the sedimentation momentum fluxes, with only a minor increase in the coefficient of friction in the latter case. This illustrates that these momentum fluxes do not dominate the simulated flow behavior.

#### IV. DISCUSSION

The model presented here can simulate both the static and internal flowing regions observed in granular column collapses. The broad scaling laws are captured. The model provides fits to observations with values of the coefficient of friction ( $\mu=0.4$ ) that are in agreement with laboratory measurements.

Minor differences between these simulations and observations, however, remain. The observed scaled deposit profiles are steeper than those simulated. This over-concavity of the final simulated profile was also observed by Balmforth and Kerswell<sup>3</sup> and appears inherent to the shallow water model. The increased curvature exists in a region beyond the static wedge, and thus is likely to arise from an oversimplified treatment of sedimentation or friction.

The variations in the values of  $L_s$  and  $\mu$  assumed affect the form of the simulated interface between the static and flowing regions. The free surface shape of the deposit is thus affected to a greater degree in the later stages of propagation as this interface moves closer to the free surface. Increasing the coefficient of friction in the modeled flowing layer, which encompasses a thin shear layer, steepens the final profile. A higher value of  $L_s$  reduces the overconcavity. However, these changes result in a reduction in both the velocity and the final runtime of the flow, inconsistent with experimental observations.

There are velocity differences between the simulated scaled run-out profile and observations for both  $a=5$  and 7 [Fig. 8(d)], reflected in the low prefactor found for the time scaling law [Eq. (26)]. This model assumes constant sedimentation and constant friction. However, experiments<sup>16</sup> show two stages of sedimentation, with a higher  $L_s$  during the column collapse phase. Thus a trial investigation, defining the sedimentation in the free fall phase ( $t < t_r$ ) as  $L_{s1} = 0.35$  m/s and in the lateral spreading phase ( $t > t_r$ ) as  $L_{s2} = 0.5L_{s1}$  was conducted.

This two stage sedimentation results in a steeper simulated deposit from the back of the lock to beyond the initial wedge location, due to the initially higher sedimentation. The lower sedimentation in the lateral spreading phase reduces the deposit angle near the flow front. Thus, the curvature of the final profile is reduced considerably and the differences between observed and simulated deposits are improved when compared to simulations with a constant sedimentation rate. Experimental studies<sup>16</sup> also indicate that this sedimentation rate may have a shear rate dependence, which could be incorporated into the model in the manner of Douady *et al.*<sup>24</sup> or via the dimensionless shear rate parameter  $I$  of MIDI.<sup>34</sup> Quantification of the dependence of the sedimentation  $L_s$  on aspect ratio  $a$ , distance  $x$ , and time  $t$ , constrained in the laboratory, should allow a variable  $L_s$  to be incorporated into the existing model.

The shallow water model cannot capture final avalanching of these flows. In addition, Lube *et al.*<sup>16</sup> observe an increase in total area of the deposit at time  $t_\infty$  compared to  $t_o$ . This dilation behavior is not possible in our model framework. Modeling the expansion of the flow may reduce the discrepancy seen between the observed and final free surface profiles [Fig. 8(f)]. With the current assumptions of constant sedimentation and no vertical variations, one would not expect to capture all the characteristics of the flows, however capturing the key features is a major improvement on earlier studies. As discussed by Kerswell,<sup>13</sup> to capture the evolution of these granular column collapses, not only requires retaining two spatial dimensions and incorporating the internal material stresses, but also requires acknowledgment that the material dilates and contracts during its motion.

## V. CONCLUDING REMARKS

In this work we have extended the model of Larrieu *et al.*<sup>14</sup> for granular column collapse to include an estimation for the interface between the static and flowing regions observed in these collapses by Lube *et al.*<sup>16</sup> The model of Larrieu *et al.*,<sup>14</sup> while capturing the free surface flows and key scaling laws for  $a < 10$ , requires a very high coefficient of friction ( $\mu=0.9$ ) to reproduce run-outs observed.<sup>1</sup> The model also fails for high aspect ratio columns. We address these issues by modeling the collapse with two layers, one static and one flowing. The interface between them provides the basal topography for the flowing layer which grows due to the introduction of a sedimentation term  $L_s$ .

Introducing this sedimentation improves upon Larrieu *et al.*<sup>14</sup> as simulations are more consistent with what is physically observed in the internal regions of these flows. In addition, a smaller value of dynamic friction ( $\mu=0.4$ ) representative of quartz sand measured independently in other laboratory studies (Table I), produces simulations closest to observations when a constant sedimentation rate of  $L_s = 0.20$  m/s is imposed. This sedimentation rate is within the range observed for the rise of the static region surface.<sup>16</sup> However, a problem emerges when the times at which the flow front stops  $t_{xf}$  and when all material is sedimented into the static deposit  $t_\infty$  are considered. All material is finally sedimented after the flow front stops. This is unphysical and inconsistent with observations, which show that the flow front stops when the static surface reaches the free surface.

To address this issue, a deposit wedge corresponding to the initial static wedge observed in experiments is introduced. Instantaneous removal of this wedge occurs at  $t_w$  when the layer height  $h$  reaches the critical wedge apex height. This initial static wedge has been neglected in previous models, and its presence dramatically improves the simulated run-out. In addition, the deposit and flowing layer profiles are smoother and more comparable to the observations of Lube *et al.*<sup>16</sup> (Fig. 1).

For  $a > 3$  the key scaling laws for final run-out time upon  $a^{0.5}$  and the run-out distance  $a^{2/3}$  are captured. With previous models this has not been possible for tall columns where  $a \geq 10$ . As stated by Larrieu *et al.*,<sup>14</sup> their model required just the use of a basal friction and mass addition to

capture the free surface and run-out of these collapses. With the introduction of just one more ingredient, mass loss, we also capture both the static and flowing regions and run-out behavior for tall columns. The application of this extends beyond observed and simulated collapses, to larger sedimenting high concentrated debris flows and the consideration of sedimentation from a dense basal layer of hazardous pyroclastic flows useful in the development of large mechanistic numerical models utilized in hazard assessment.

## ACKNOWLEDGMENTS

E.E.D. was supported by a UK Natural Environment Research Council Ph.D. Grant No. NER/S/A/2003/11201 and would like to acknowledge the advice of Dr. Andy Hogg with regards to theoretical development of granular and debris flow theory.

G.L. acknowledges support by the Deutsche Forschungsgemeinschaft (Grant Nos. Fr 947/9-1 and 9-2) and a David-Crichton Fellowship.

The research of H.E.H. and R.S.J.S. is supported by the Royal Society Wolfson Research Merit Awards.

- <sup>1</sup>G. Lube, H. E. Huppert, R. S. J. Sparks, and M. A. Hallworth, "Axisymmetric collapses of granular columns," *J. Fluid Mech.* **508**, 175 (2004).
- <sup>2</sup>E. Lajeunesse, A. Mangeney-Castelnau, and J. P. Vilotte, "Spreading of a granular mass on a horizontal plane," *Phys. Fluids* **16**, 2371 (2004).
- <sup>3</sup>N. J. Balmforth and R. R. Kerswell, "Granular collapse in two dimensions," *J. Fluid Mech.* **538**, 399 (2005).
- <sup>4</sup>G. Lube, H. E. Huppert, R. S. J. Sparks, and A. Freundt, "Collapses of two-dimensional granular columns," *Phys. Rev. E* **72**, 041301 (2005).
- <sup>5</sup>C. S. Campbell and C. E. Brennen, "Computer simulation of granular shear flows," *J. Fluid Mech.* **151**, 167 (1985).
- <sup>6</sup>L. Staron and E. J. Hinch, "Study of the collapse of granular columns using 2D discrete-grains simulation," *J. Fluid Mech.* **545**, 1 (2005).
- <sup>7</sup>R. Zenit, "Computer simulations of the collapse of a granular column," *Phys. Fluids* **17**, 031703 (2005).
- <sup>8</sup>S. B. Savage and K. Hutter, "The motion of a finite mass of granular material down a rough incline," *J. Fluid Mech.* **199**, 177 (1989).
- <sup>9</sup>K. Hutter, M. Siegel, S. B. Savage, and Y. Nohguchi, "Two-dimensional spreading of a granular avalanche down an inclined plane," *Acta Math. Acad. Sci. Hung.* **100**, 37 (1993).
- <sup>10</sup>O. Pouliquen and Y. Forterre, "Friction law for dense granular flows: Application to the motion of a mass down a rough inclined plane," *J. Fluid Mech.* **453**, 133 (2002).
- <sup>11</sup>A. Mangeney-Castelnau, J. P. Vilotte, M. O. Bristeau, B. Perthame, F. Bouchut, C. Simeoni, and S. Yerneni, "Numerical modeling of avalanches based on saint venant equations using a kinetic scheme," *J. Geophys. Res.* **108**, 2527, DOI:10.1029/2002JB002024 (2003).
- <sup>12</sup>A. Mangeney-Castelnau, F. Bouchut, J. P. Vilotte, E. Lajeunesse, and A. Aubertin, "On the use of Saint-Venant equations for simulating the spreading of a granular mass," *J. Geophys. Res., [Solid Earth]* **110**, B09103, DOI:10.1029/2004JB003161 (2005).
- <sup>13</sup>R. R. Kerswell, "Dam break with coulomb friction: A model for granular slumping?" *Phys. Fluids* **17**, 057101 (2005).
- <sup>14</sup>E. Larrieu, L. Staron, and E. Hinch, "Raining into shallow water as a description of the collapse of a column of grains," *J. Fluid Mech.* **554**, 259 (2006).
- <sup>15</sup>O. Pouliquen, "Scaling laws in granular flows down rough inclined planes," *Phys. Fluids* **11**, 542 (1999).
- <sup>16</sup>G. Lube, H. E. Huppert, R. S. J. Sparks, and A. Freundt, "Static and flowing regions in granular collapses down channels," *Phys. Fluids* **19**, 043301 (2007).
- <sup>17</sup>J. Gray, "Granular flow in partially filled slowly rotating drums," *J. Fluid Mech.* **441**, 1 (2001).
- <sup>18</sup>M. A. Carrigy, "Experiments on the angles of repose of granular materials," *Sedimentology* **14**, 147 (1970).
- <sup>19</sup>O. Hungar and N. R. Morgenstern, "Experiments on the flow behaviour of

- granular materials at high velocity in an open channel," *Geotechnique* **34**, 405 (1984).
- <sup>20</sup>B. Cagnoli and M. Manga, "Granular mass flows and Coulomb's friction in shear cell experiments: Implications for geophysical flows," *J. Geophys. Res.* **109**, F04005, DOI:10.1029/2004JF000177 (2004).
- <sup>21</sup>Z. Chik and L. E. Vallejo, "Characterization of the angle of repose of binary granular materials," *Can. Geotech. J.* **42**, 683 (2005).
- <sup>22</sup>A. Mangeney, P. Heinrich, and R. Roche, "Analytical solution for testing debris avalanche and numerical models," *Pure Appl. Geophys.* **157**, 1081 (2000).
- <sup>23</sup>P. Jop, Y. Forterre, and O. Pouliquen, "A constitutive law for dense granular flows," *Nature (London)* **441**, 727 (2006).
- <sup>24</sup>S. Douady, B. Androetti, and A. Daerr, "On granular surface flow equations," *Eur. Phys. J. B* **11**, 131 (1999).
- <sup>25</sup>M. Ungarish and H. E. Huppert, "The effects of rotation on axisymmetric gravity currents," *J. Fluid Mech.* **362**, 17 (1998).
- <sup>26</sup>A. J. Hogg and D. Pritchard, "The effects of hydraulic resistance on dam-break and other shallow inertial flows," *J. Fluid Mech.* **501**, 179 (2004).
- <sup>27</sup>H. Huppert, "Quantitative modelling of granular suspension flows," *Philos. Trans. R. Soc. London, Ser. A* **356**, 2471 (1998).
- <sup>28</sup>R. J. Leveque, *Finite Volume Methods for Hyperbolic Problems*, Cambridge Texts in Applied Mathematics (Cambridge University Press, Cambridge, 2002).
- <sup>29</sup>R. P. Denlinger and R. M. Iverson, "Granular avalanches across irregular three-dimensional terrain: 1. Theory and computation," *J. Geophys. Res.* **109**, F01014, DOI:10.1029/2003JF000085 (2004).
- <sup>30</sup>The TRBDF2 formula is erroneous in Leveque (Ref. 28), and should be  $Q_i^{**} = Q_i^* + (\Delta t/4)[\psi(Q_i^*) + \psi(Q_i^{**})]$  and  $Q_i^{n+1} = \frac{1}{3}[4Q_i^{**} - Q_i^* + \Delta t\psi(Q_i^{n+1})]$  for the stiff ordinary differential equation  $q_t = \psi(q)$ , where  $Q$  is the solution sought at time step  $n+1$  and grid  $i$ .
- <sup>31</sup>M. E. Hubbard and P. Garcia-Navarro, "Flux difference splitting and the balancing of source terms and flux gradients," *J. Comput. Phys.* **165**, 89 (2000).
- <sup>32</sup>R. Leveque, "Balancing source terms and flux gradients in high-resolution Godunov methods: The quasisteady wave propagation algorithm," *J. Comput. Phys.* **146**, 346 (1998).
- <sup>33</sup>V. Caleffi, A. Valiani, and A. Zanni, "Finite volume method for simulating extreme flood events in natural channels," *J. Hydraul. Res.* **41**, 167 (2003).
- <sup>34</sup>G. D. R. MIDI, "On dense granular flows," *Eur. Phys. J. E* **14**, 341 (2004).
- <sup>35</sup>A. Suzuki and T. Tanaka, "Measurement of flow properties of powders along an inclined plane," *Ind. Eng. Chem. Fundam.* **10**, 84 (1971).
- <sup>36</sup>H. Ahn, C. E. Brennen, and R. H. Sabersky, "Measurements of velocity, velocity fluctuation, density and stresses in chute flows of granular materials," *ASME J. Appl. Mech.* **58**, 793 (1991).
- <sup>37</sup>J. S. Patton, C. E. Brennen, and R. H. Sabersky, "Shear flows of rapidly flowing granular materials," *ASME J. Appl. Mech.* **54**, 801 (1987).
- <sup>38</sup>J. M. N. T. Gray, M. Wieland, and K. Hutter, "Gravity-driven free surface flow of granular avalanches over complex basal topography," *Proc. R. Soc. London, Ser. A* **455**, 1841 (1999).
- <sup>39</sup>J. Lohrmann, N. Kukowski, J. Adam, and O. Oncken, "The impact of analogue material properties on the geometry, kinematics and dynamics of convergent sand wedges," *J. Struct. Geol.* **25**, 1691 (2003).
- <sup>40</sup>O. Hungr and N. R. Morgenstern, "High velocity ring shear tests on sand," *Geotechnique* **34**, 415 (1984).
- <sup>41</sup>S. De Toni and P. Scotton, "Two-dimensional mathematical and numerical model for the dynamics of granular avalanches," *Cold Regions Sci. Technol.* **43**, 36 (2005).